Dominant patterns of interaction between the tropics and mid-latitudes in boreal summer: Causal relationships and the role of time-scales

Giorgia Di Capua[1,2], Jakob Runge[3], Reik V. Donner[1,4], Bart van den Hurk[2,5], Andrew G. Turner[6,7], Ramesh Vellore[8], Raghavan Krishnan[8], and Dim Coumou[1,2]

[1]Potsdam Institute for Climate Impact Research, Potsdam, Germany
[2]VU University of Amsterdam, Institute for Environmental Studies, Amsterdam, Netherlands
[3]German Aerospace Centre, Institute of Data Science, Jena, Germany
[4]Magdeburg-Stendal University of Applied Sciences, Magdeburg, Germany
[5]Deltares, Delft, Netherlands
[6]Department of Meteorology, University of Reading, Reading, United Kingdom
[7]National Centre for Atmospheric Science, University of Reading, Reading, United Kingdom
[8]Indian Institute for Tropical Meteorology, Pune, India

Correspondence to: Giorgia Di Capua (dicapua@pik-potsdam.de)

Abstract.   Tropical convective activity represents a source of predictability for mid-latitude weather in the Northern Hemisphere. In winter, the El Niño–Southern Oscillation (ENSO) is the dominant source of predictability in the tropics and extra-tropics, but its role in summer is much less pronounced and the exact teleconnection pathways are not well understood. Here, we assess how tropical convection interacts with mid-latitude summer circulation at different intraseasonal time-scales and how ENSO affects these interactions. First, we apply maximum covariance analysis (MCA) between tropical convective activity and mid-latitude geopotential height fields to identify the dominant modes of interaction. The first MCA mode connects the South Asian monsoon with the mid-latitude circumglobal teleconnection pattern. The second MCA mode connects the western North Pacific summer monsoon in the tropics with a wave-5 pattern centred over the North Pacific High in the mid-latitudes. We show that the MCA patterns are fairly insensitive to the selected intraseasonal time-scale from weekly to 4-weekly data. To study the potential causal interdependencies between these modes and with other atmospheric fields, we apply causal effect networks (CEN) at different time-scales. CENs extend standard correlation analysis by removing the confounding effects of autocorrelation, indirect links and common drivers. In general, there is a two-way causal interaction between the tropics and mid-latitudes but the strength and sometimes sign of the causal link are time-scale dependent. We introduce causal maps that plot the regionally specific causal effect from each MCA mode. Those maps confirm the dominant patterns of interaction and in addition, highlight specific mid-latitude regions that are most strongly connected to tropical convection. In general, the identified causal teleconnection patterns are only mildly affected by ENSO and the tropical-mid-latitude linkages remain similar. Still, La Niña strengthens the South Asian monsoon generating a stronger response in the mid-latitudes, while during El Niño years, the Pacific pattern is reinforced. This study paves the way for process-based validation of boreal summer teleconnections in (sub-)seasonal forecast models and climate models and therefore helps to improve sub-seasonal and climate projections.

1 Introduction

Tropical – mid-latitude teleconnections in boreal summer can have a great impact on surface weather conditions in the northern mid-latitudes (Ding and Wang, 2005; O'Reilly et al., 2018; Wang et al., 2001). Still, the direct influence of the El Niño-Southern Oscillation (ENSO) on the mid-latitude circulation is weaker in summer than in winter (Branstator, 2002; Schubert et al., 2011; Thomson and Vallis, 2018). Instead, in summer, convective activity related to the Northern Hemisphere tropical monsoon systems can profoundly influence surface weather conditions in the mid-latitudes (Branstator, 2014; Ding and Wang, 2005; O'Reilly et al., 2018; Rodwell and Hoskins, 1996). Vice versa, mid-latitude wave trains and cyclonic activity at intraseasonal time-scales can modulate the tropical monsoons, and have been linked to extreme rainfall events in the Indian region (Lau and Kim, 2011; Vellore et al., 2014, 2016). Therefore, tropical and mid-latitude regions are likely connected in

complex, two-way, teleconnection patterns operating at a range of sub-seasonal time-scales (Di Capua et al., 2020; Ding and Wang, 2005, 2007).

During boreal summer, the South Asian monsoon (SAM), represents one of the most important and powerful features of the
70   tropical/subtropical circulation. Characterized by heavy rainfall over central India and the Bay of Bengal, the SAM has strong intraseasonal variability associated with alternating active and break phases, linked to the boreal summer intraseasonal oscillation (BSISO, Choudhury and Krishnan, 2011; Gadgil and Joseph, 2003; Goswami et al., 1998; Krishnamurti and Surgi, 1987; Krishnan et al., 2000; Rao, 1976; Saha et al., 2012; Suhas et al., 2012). The western North Pacific summer monsoon (WNPSM) represents the Pacific counterpart to the SAM and is identified by strong rainfall over the sub-tropical North Pacific
75   (Li and Wang, 2005). Similar to the SAM, the WNPSM also exhibits strong intraseasonal oscillations (Wang and Xu, 1997). Latent heat release due to strong monsoonal rainfall can influence subtropical and mid-latitude regions via Rossby wave teleconnections. The SAM has been connected to subtropical arid conditions in the North African region via the so-called monsoon – desert mechanism, creating reinforced descending motions over the Sahara during strong SAM phases (Rodwell and Hoskins, 1996; Stephan et al., 2019). This mechanism is fairly well captured by both climate (Cherchi et al., 2014) and
80   seasonal forecast models (Beverley et al., 2019).The SAM is also connected to mid-latitude circulation via its interaction with the circumglobal teleconnection pattern (CGT), a wave pattern with 5 centres of action encircling the northern mid-latitudes and affecting temperature and precipitation there (Ding and Wang, 2005; Kripalani et al., 1997). This wave-5 like CGT pattern can be identified through interannual to intraseasonal (weekly) time-scales and it is likely connected with the SAM via two-way causal links (Di Capua et al., 2020). Seasonal forecast models are biased in their representation of the CGT, with typically
85   a too weak CGT signal (Beverley et al., 2019). Therefore, seasonal forecasts miss an important source of predictability on intraseasonal time-scales, primarily in summer (Weisheimer and Palmer, 2014).

The WNPSM has been shown to influence precipitation anomalies over North America via its relation to the Western Pacific – North America (WPNA) pattern (Wang et al., 2001). The WNPSM is shown to be related to surface pressure conditions over East Asia, with high pressure anomalies during years characterized by stronger WNPSM activity (Nitta, 1987). The WNPSM
90   area also represents a genesis region for tropical cyclones in the North Pacific (Briegel and Frank, 1997). The WNPSM is weaker during the decaying phase of El Niño (Wang et al., 2001) and its related circulation anomalies provide a link from ENSO to the East Asia summer monsoon (EASM) (Yim et al., 2008). Thus, in summary, the SAM appears particularly important for sub-seasonal variability over Eurasia, while the WNPSM is important for the Pacific-North American sector.

ENSO, operating at interannual time-scales, might primarily influence the mid-latitude circulation via its effect on the SAM
95   strength (Ding et al., 2011). During boreal summers preceding La Niña phases, a strengthening of the Walker circulation can enhance SAM rainfall, while El Niño phases often have an opposite effect (Joseph et al., 2011; Ju and Slingo, 1995; Terray et al., 2003; Wu et al., 2012). However, this relationship depends on the longitudinal position of the strongest El Niño related sea surface temperature (SST) anomalies (Krishna Kumar et al., 2006) and potentially has weakened over recent decades (Chakraborty and Krishnamurti, 2003; Krishna Kumar et al., 1999; Srivastava et al., 2017; Xavier et al., 2007). At interannual
100   time-scales, anomalous tropical convection in the central-eastern Pacific related to ENSO has also been shown to affect mid-

latitude circulation over the Euro-Atlantic sector as well as temperature and precipitation anomalies over Europe during boreal summer (O'Reilly et al., 2018). Trends in tropical SSTs play a crucial role in the interdecadal changes of this tropical-extratropical teleconnection (O'Reilly et al., 2019).

In general, a major challenge faced by teleconnection research is to understand the underlying physical processes and associated cause-effect relationships. Past observational studies have typically employed correlation analysis or linear regression techniques. Such analyses can however be dominated by spurious correlations and therefore can give only limited insight into cause-effect relationships. On the other hand, model-based studies can be affected by biases in the representation of circulation and precipitation characteristics (Beverley et al., 2019; Schubert et al., 2011; Weisheimer and Palmer, 2014), which can feed back on each other. Also, although perturbation and sensitivity experiments can point towards potential causal relationships, they do not necessarily reveal the causal links between tropical and mid-latitudinal features, since the uncovered relationship may not be the dominant one.

Here, we apply a causal discovery approach making use of the so-called PCMCI (Peter & Clark algorithm combined with the Momentary Conditional Independence approach, see Section 2.3) method (Runge et al., 2019). This method detects causal links and Causal Effect Networks (CEN) (Kretschmer et al., 2016) to quantify their effect strength, in order to study the relationships between the Northern Hemisphere mid-latitudes and the tropical belt during boreal summer at different intraseasonal time-scales. Expanding our understanding of these mechanisms has the potential to improve seasonal and subseasonal forecasts in boreal summer. The main advantage of such tools is that they can identify and remove spurious correlations (Runge, 2018; Runge et al., 2015b, 2019) and thus provide insight into the potential causal relationships (McGraw and Barnes, 2018; Runge et al., 2014). Building upon this advanced methodology, we introduce a new concept called causal maps, identifying causally related spatial structures. Finally, we assess the role of the ENSO background state on the identified causal relationships between the tropical belt and the mid-latitude circulation. The remainder of this paper is organized as follows: Section 2 presents the data and methods used in this analysis. Section 3 describes the results obtained by applying CEN and causal maps to the identified research questions. Section 4 illustrates the discussion of the obtained results in the context of the existing literature and finally, Section 5 presents a short summary and conclusions.

2 Data and Methods

2.1 Data

In our analysis, we diagnose monsoon characteristics and Northern Hemisphere circulation features using outgoing longwave radiation (OLR) at the top of the atmosphere, geopotential height at 200 hPa (Z200) and 2m surface temperature (T2m) data from the ERA-Interim Reanalysis (Dee et al., 2011) for the period 1979-2018 (1.5°x1.5°). Strong tropical convection is characterized by high cloud tops and thus by low emission temperatures, which in turn correspond to low OLR values (Krishnan et al., 2000). In the tropical belt, OLR can be used as a proxy of convective activity, and therefore, rainfall. To select different ENSO phases, we use the monthly Niño3.4 index from NOAA (data are available at

https://www.esrl.noaa.gov/psd/gcos_wgsp/Timeseries/Nino34/), representing the central Pacific SST anomalies. El Niño and La Niña events are discerned by periods of December-to-February Niño3.4 index values larger than 0.5°C or smaller than -

135   0.5°C respectively. Then, we identify El Niño summers as those preceding the El Niño peak in winter and La Niña summers as those preceding the La Niña peak in winter. We use the Niño3.4 index since it has been shown to have a relatively strong connection to Indian monsoon rainfall (Krishna Kumar et al., 2006).

We also use the BSISO index as defined by Kikuchi et al. (2012) and Kikuchi and Wang (2010) (data are available at http://iprc.soest.hawaii.edu/users/kazuyosh/ISO_index/data/BSISO_25-90bpfil_pc.txt) in order to describe the phase and

140   amplitude of the BSISO characterising the large-scale driver of active and break events over India. Causal discovery tool techniques require detrended anomalies centred at zero. Therefore, all data are linearly detrended and anomalies are calculated relative to an individual year's mean seasonal state by removing both the mean seasonal cycle and the year's mean seasonal state (i.e. the seasonal average from May to September, MJJAS) (Di Capua et al., 2020; Ding and Wang, 2007). Removing the year's mean seasonal state, and thus excluding the influence of interannual variations of the involved mechanisms, is essential

145   to analyse intraseasonal variability of atmospheric components that present a strong interannual variably, such as the SAM.

2.2 Maximum covariance analysis

To extract the dominant co-variability patterns reflecting interactions between the tropics and mid-latitude, we first apply maximum covariance analysis (MCA) to tropical OLR (15°S-30°N, 0°-360°E) and northern mid-latitude Z200 (25°N-75°N,

150   0°-360°E) fields. MCA identifies the patterns that explain the *greatest squared covariance between two different fields* (Ding et al., 2011; Wiedermann et al., 2017) and ranks them according to their explained squared covariance fraction (SCF) (Wilks, 2011). Each MCA mode thus provides two coupled (2D) spatial patterns (one for tropical OLR and one for mid-latitude Z200) and two associated (1D) time series (the time-dependent MCA scores or pattern amplitudes for both fields), describing the magnitude (prominence) and phase (sign) of those patterns for each time step. These (1D) time series are obtained by

155   calculating the scalar product between each MCA spatial pattern (2D field) and the original spatial field of the associated variable at each time step as

$$A = \boldsymbol{u}^T \boldsymbol{X} \qquad (1)$$

$$B = \boldsymbol{v}^T \boldsymbol{Y} \qquad (2)$$

where A and B represent the two MCA scores for Z200 and OLR, $\boldsymbol{X}$ and $\boldsymbol{Y}$ are two matrices representing Z200 and OLR fields,

160    $\boldsymbol{u}$ and $\boldsymbol{v}$ are the coupled patterns that maximize their covariance c, defined as:

$$c = cov[A, B] = cov[\boldsymbol{u}^T \boldsymbol{X}, \boldsymbol{v}^T \boldsymbol{Y}] = \frac{1}{n-1}[\boldsymbol{u}^T \boldsymbol{X}(\boldsymbol{v}^T \boldsymbol{Y})^T] = \boldsymbol{u}^T \boldsymbol{C}_{xy} \boldsymbol{v} \qquad (3)$$

and

$$\boldsymbol{C}_{xy} = \frac{1}{n-1} \boldsymbol{X} \boldsymbol{Y}^T \qquad (4)$$

with n denoting the number of observation times.

165

2.3 PCMCI and Causal Effect Networks

PCMCI is a causal discovery method based on the PC algorithm (named after its inventors Peter and Clark, see Spirtes et al., 2000) combined with the Momentary Conditional Independence approach (MCI, Runge et al., 2019). Given a set of univariate time series (called *actors*), PCMCI estimates their time series graph that represents the conditional independencies among the time-lagged actors. In the context of the present work, actors are user-selected based on theoretical knowledge to represent either a specific component of the atmospheric circulation or surface conditions estimated with MCA (*A*, *B*) or an individual grid point time series *C*(lat, lon). Assuming linear dependencies, PCMCI uses partial correlations to iteratively test conditional independencies and remove spurious links arising from autocorrelation effects, indirect links, or common drivers. For example, if an actor *Z* drives *X* at lag -1 and *Y* at lag -2, then *X* and *Y* will be correlated, but the partial correlation $\rho(X_{t-1}, Y_t \mid Z_{t-2})$ will be zero. PCMCI efficiently conducts partial correlation tests to identify which links cannot be explained by other time-lagged actors. Compared to the standard PC algorithm, PCMCI better deals with autocorrelation and high-dimensional sets of actors (Runge et al., 2019). The output of PCMCI is a *p*-value for each time-lagged causal link.

It is important to note that the term causal rests on specific assumptions (Runge, 2018; Spirtes et al., 2000), most importantly that it should be understood as "causal relative to the set of analysed actors". Therefore, adding (or removing) an actor can alter the result of PCMCI, highlighting the importance of having an expert-guided hypothesis underlying the choice of the selected set of actors. In addition, using partial correlation for a conditional independence test implies further assumptions such as the stationarity and linearity of the relationships. To ensure that multiple testing does not inflate *p*-values or the multiple grid locations in causal maps, we apply the false discovery rate (FDR) correction (Benjamini and Hochberg, 1995).

Based on the reconstructed network among the actor variables (at some significance level α), we determine the causal parents as the incoming links to each actor (*C*(lat, lon), *A*, *B*), which can come from the pasts of *A*, *B*, or *C*(lat, lon) , i.e., { A_{t-1}, B_{t-1}, C(lat, lon) $_{t-1}$, ... , $A_{t-\tau max}$, $B_{t-\tau max}$, C(lat, lon) $_{t-\tau max}$}. Then we estimate the Causal Effect Network (CEN) (Kretschmer et al., 2016; Runge et al., 2015a) among *A*, *B* and *C*(lat, lon) by applying standardized multiple regression of each actor onto its parents, i.e., for *Y* ∈ in A_t, B_t, *C*(lat, lon)$_t$ and the parents *P*:

$$Y_t = \sum_i \beta_i X_i + \eta_Y \tag{5}$$

190

where $X_i \in P\{Y\}$, *i* = 1, .., *N*, i.e. the set of *N* parents of *Y*. Note that there can be different numbers *N* of parents for each actor. Finally, the strength of a causal link $X_{t-\tau} \rightarrow Y_t$ is expressed in terms of the path coefficient *β*, which can be interpreted as the change in the expectation of Y_t (in units of its standard deviation (s.d.)) induced by raising $X_{t-\tau}$ by 1 s.d., while keeping all other parents of Y_t constant. Thus, for *β* = 0.5, a change in a causal parent of 1 s.d. at lag -1 corresponds to a change 0.5 s.d. in the analysed actor at lag 0 (Runge et al., 2015a). The influence of an actor on itself is referred to as the autocorrelation path coefficient, which must not be confused with the Pearson autocorrelation. A detailed description of the PCMCI algorithm is

available in Runge et al. (2019), while recent applications can be found in Kretschmer et al. (2016, 2018) and Di Capua et al. (2019).

2.4 Causal maps

To explore the causal effects that a specific actor has on a selected 3D (lat, lon, time) atmospheric field, we introduce the concept of *causal maps*. Conceptually, causal maps are similar to correlation maps, as they show the spatial pattern of the relationship between a 3D climate data set (covering two spatial dimensions plus time) and a 1D time series. However, instead of computing correlations between the time variations at each grid point and *one* additional time series, we apply here the PCMCI+CEN approach with actors consisting of the two MCA scores time series (*A*, *B*) and each individual grid point time series (*C*(lat, lon)). The causal map then plots the path coefficient *β* from one of the MCA scores (as one actor) to this gridpoint, conditioned on all remaining actors. For a set of two actor timeseries (*A* and *B* in Fig. 1) and one time-varying atmospheric field *C*, we can thus derive two causal maps: one from *A* to *C*(lat, lon) conditioned on *B* and on the autocorrelation in all actors, and one from *B* to *C*(lat, lon) conditioned on *A* and on all autocorrelation effects. Figure 1 provides an illustrative example of this type of analysis. Both correlation maps (Fig. 1a) indicate a positive value for a specific geographical location highlighted with the black diamond. The CEN constructed for *A*, *B* and *C*(lat, lon) at this gridpoint is plotted in Fig. 1b and shows that only *B* is causally connected to *C*. The correlation between *A* and *C* is thus due to an indirect link via *B* (or to a common driver not included in the CEN). This is also seen in the causal maps plotting the path coefficient *β* which for the *B* → *C*(lat, lon) link is positive (right panel) but is non-significant for the *A* → *C*(lat, lon) link (left panel). In causal map visualization we can directly illustrate the effect of a specific actor on a global field (taking into account the influence of autocorrelation), indirect links and common driver effects due to other competing variables.

3 Results

3.1 Tropical – mid-latitude interactions: maximum covariance analysis

To analyse the interactions between mid-latitude circulation in the Northern Hemisphere and tropical convection at intraseasonal time-scales, we follow Ding et al. (2011) and apply maximum covariance analysis (MCA) to OLR fields (used as a proxy for convective activity) in the tropical belt (defined as 15°S-30°N, 0-360°E) paired with Z200 fields in the northern mid-latitudes (25-75°N, 0-360°E). Here, we select the first two MCA modes as representing the most important co-variability patterns between tropical convection and mid-latitude circulation. Figures 2a-d show the coupled patterns for the first two MCA modes between weekly tropical OLR and mid-latitude Z200. Figure 2e shows the associated time series of MCA scores for all four patterns (two for each MCA mode).

The first two MCA modes highlight the two key patterns of monsoonal activity in the tropics along with the co-varying mid-latitude Z200 patterns. In both modes, the mid-latitudes are characterized by a zonally oriented circumglobal wave pattern

with a wavenumber close to 5 (i.e. roughly 5 centres of action). However, the two wave patterns are phase shifted, aligned with the longitudinal position of the strongest monsoonal convection in the tropics.

230   The first MCA mode explains 18% of the squared covariance (squared covariance fraction, SCF) and shows a CGT-like wave-5 pattern (the spatial correlation with the weekly CGT pattern, as defined by Ding and Wang 2005, is 0.52) in mid-latitude Z200 (Fig. 2a). The CGT co-varies with a band of enhanced tropical convective activity that extends from the Arabian Sea towards Southeast Asia, with a peak of convective activity over the Bay of Bengal (Fig. 2b) (Kang et al., 1999). We will refer to this pattern as the South Asian monsoon (SAM). Note that we name each MCA pattern after a characteristic regional feature,

235   but the analysis is applied to the larger geographical domains as shown in Figure 2. The Pearson correlation between the two time series of MCA scores for the first mode is r ~ 0.5.

The second mode of co-variability explains a SCF of 14% between the two fields and is characterized by a region of strong positive Z200 anomalies located at ~ 45° N, over the western North Pacific, directly to the west of the dateline (i.e. the most prominent centre of action of the mid-latitude wave). We will refer to this pattern as the North Pacific High (NPH) (Fig. 2c).

240   The NPH is the summer counterpart of the North Pacific subtropical high, which characterizes boreal winter. During summer, this high pressure region is displaced northward replacing the Aleutian Low (Lu, 2001; Riyu, 2002). As can be seen in MCA mode 1, the NPH is associated with a region of enhanced convection over the sub-tropical western North Pacific, related to the western North Pacific summer monsoon (WNPSM) convective activity (Fig. 2d) (Li and Wang, 2005; Nitta, 1987; Wang et al., 2001). The Pearson correlation between the two time series of MCA scores for the first mode is r ~ 0.6.

245   Application of the MCA to 4-weekly data gives nearly identical MCA patterns but with somewhat lower magnitude of the Z200 and ORL anomalies (see Fig. S1 in the Supplementary Material). In this case, we define both 4-weekly and weekly MCA scores by projecting 4-weekly MCA patterns onto 4-weekly and weekly data respectively (see Fig. S1e-f in the Supplementary Material). In this way, we check whether the analysis is robust given different definitions of the MCA patterns.

Using OLR composites, we explicitly show that the temporal evolution of the SAM convective activity at weekly time-scales

250   resembles the evolution of the Boreal Summer Intraseasonal Oscillation (BSISO) (Goswami and Ajaya Mohan, 2001; Saha et al., 2012) (see Fig. S2 in the Supplementary Material). The OLR pattern depicted by the first MCA mode represents phase 4-5 of the BSISO evolution (Fig. S2). The BSISO is characterized by a rainfall band tilted from northeast to southwest propagating from the tropical Indian Ocean toward Southeast Asia with a period of about one to two months. To further explore this hypothesis, we present a Wheeler-Hendon diagram using the BSISO index as defined by Kikuchi (2010) and plot (using

255   different colours) BSISO phases that correspond to different lags (as defined considering the MCA mode 1 pattern for OLR as lag 0, see Fig. S2). The results show that each lag tends to cluster consistently around the corresponding BSISO phase (see Fig. S3a in the Supplementary Material). This suggests that the BSISO may exert a large-scale tropical control on mid-latitude anomalies, using variations in SAM rainfall as a pathway. When the same approach is applied to the WNPSM pattern, no consistent behaviour can be identified (Fig. S3b).

3.2 Influence of tropical – mid-latitude MCA modes on Northern Hemisphere circulation

To show how each MCA mode affects the circulation and surface conditions in the Northern Hemisphere, we calculate causal maps for the influence of SAM, CGT, WNPSM and NPH time series (as defined in Fig. 2e) on selected atmospheric fields in the Northern Hemisphere (15°S-75°N, 0°-360°E). Although we use τ_{max} = -4 and τ_{min} = 0, we plot only β values for lag -1 (week), as β values for longer time lags are mostly nonsignificant. This way also the past behaviour of each actor, with potential confounding effects, is accounted for in the corresponding grid-point CEN.

Figure 3 shows the causal maps for weekly Z200 fields with SAM and CGT time series, including correlation maps for weekly Z200 fields with SAM and CGT time series. In the mid-latitudes, the correlation map between Z200 and SAM (Fig. 3a) shows a similar wave pattern as that shown in the correlation map between Z200 and CGT (Fig. 3b). Both correlation maps also display a positive correlation over northern Africa, though with smaller values in the CGT plot. The causal map for the link SAM $_{\tau = -1}$ → Z200 $_{\tau = 0}$ (after removing the effects of the CGT) shows that the path coefficient β remains pronounced over northern India and northern Africa (Fig. 3c). Interestingly, those regions disappear completely in the causal map for the link CGT $_{\tau = -1}$ → Z200 $_{\tau = 0}$ (after removing the effects from SAM). Thus, in this way, we can separate the signal coming from SAM convective activity from signals originating from the CGT pattern. Also, the causal maps in Figs. 3c and 3d indicate that the influence of SAM on Europe (negative path coefficients, Fig. 3c) and the North Pacific (Fig. 3c) is *not* mediated via the CGT. In turn, the influence of SAM on other mid-latitude regions (over some parts of East Asia and Canada/USA) is mediated via the CGT (Fig. 3d).

In the mid-latitudes, the causal maps for OLR and T2m (Figs. 3e-h) are largely consistent with those obtained for Z200, with wet anomalies (negative OLR) overlapping with colder T2m and dry anomalies (positive OLR) overlapping with warm T2m. Although the CGT influence is mostly concentrated in the mid-latitude regions, one can see a negative causal effect of the CGT pattern on OLR values over the Bay of Bengal (Fig. 3f). Again, the OLR and T2m causal maps indicate that the SAM has a direct influence on northern Africa and Europe as well as tropical Africa. Asia and North America are strongly affected by the CGT. Over the Indian peninsula and Indochina, strong convective motions (Fig. 3e) are accompanied by colder temperature (Fig. 3g), related to increased precipitation and consequently, decreased surface temperatures.

Figure 4 shows the same set of results but now for the second MCA mode consisting of WNPSM and NPH pattern related time series. As expected, both correlation maps resemble the Z200 field of MCA 2 (Fig. 2c,d) with two characteristic features: A wave-5 pattern with a prominent positive correlation over the NPH region and over western North America. The corresponding causal maps based on CENs are given in Figs. 4c (path coefficient β for the link WNPSM $_{\tau = -1}$ → Z200 $_{\tau = 0}$) and 4d (for the link NPH $_{\tau = -1}$ → Z200 $_{\tau = 0}$). If we compare the correlation maps (Figs. 4a,b) with the causal maps (Figs. 4c,d), we find great similarity in the spatial structures of the Z200 patterns over the North Pacific in both figures, although the magnitudes have reduced in Fig. 4c. These causal maps show that the influence of the WNPSM on Z200 (after removing the effect of the NPH) is confined to the North Pacific alone (Fig. 4c). The two most prominent regions displaying a significant positive path

coefficient β are found over the NPH region and over the US west coast. In contrast, the causal effect of the NPH pattern on Z200 (after removing effects of WNPSM) shows a wave train that encircles the mid-latitudes (Fig. 4d). Like the MCA mode

295   2 pattern itself, this wave train shows positive centres over Russia/Scandinavia, the western North Pacific and western US coast. The two regions in the Pacific sector coincide with those found for the WNPSM causal map (Fig. 4c). This suggests that the NPH is reinforced both by convective activity of the WNPSM and by the mid-latitude wave pattern.

Next, we compute the causal maps for the influence of WNPSM and NPH on weekly OLR and T2m fields (Figs. 4e,f and 4g,h respectively). For T2m causal maps, the results are largely consistent with those obtained for Z200, with positive Z200

300   anomalies hinting to warm and dry weather in the mid-latitudes and strong convective motions being accompanied by colder temperatures in the tropical belt. Thus, these results highlight the importance of the NPH in shaping surface temperatures across the northern mid-latitudes. The impact of the WNPSM pattern is confined to the western North Pacific. Further, convective activity in the WNPSM region is reinforced by the NPH pattern as indicated by a negative OLR anomaly over the WNPSM region (Fig. 4f). These results thus indicate that there is a two-way causal relationship between the WNPSM and the

305   NPH. Using weekly MCA scores obtained from 4-weekly MCA patterns (Fig. S1) gives consistent results, showing that the analysis is robust when a different definition of the MCA pattern is chosen (see Figs. S4-S5 in the Supplementary Material). Causal maps calculated for 4-weekly Z200 for both MCA 1 and MCA 2 show less significant results, likely due to the limited time series length (not shown).

3.3 The influence of ENSO on tropical – mid-latitude causal interactions

310   Next, we assess how the ENSO background state influences the causal relationships between mid-latitude and tropical patterns in boreal summer. To do so, we compute causal maps, similar to those in Figs. 3 and 4 but for El Niño and La Niña summers separately (Fig. 5), where El Niño (La Niña) summers are defined as summers preceding the El Niño (La Niña) peak in boreal winter. Figure S6 in the Supplementary Material shows composites of SST anomalies for summers associated with the different types of ENSO phases as defined in this way. The warm (cold) SST patterns related to El Niño (La Niña) phases are already

315   clearly developed during preceding summers, though the strongest anomalies are found in winter.

In general, the strength and the sign of the patterns seen in the causal maps (Fig. 3 and 4) are not markedly affected by ENSO, with some notable exceptions. During La Niña years, the effect of SAM on the Sahara Desert intensifies and also its effects on the Tibetan Plateau and in the mid-latitudes are more pronounced (Fig. 5c). This is likely related to stronger SAM convective activity during La Niña summers. During La Niña, we also see a few affected areas over Eurasia and North America that are

320   not present during El Niño. The region of negative causal effect of SAM on central Europe, is also present in the 1979-2018 causal map (Fig. 3c), however here the signal intensifies (and it disappears during El Niño summers). This signal is possibly linked to the strong positive causal effect over the Sahara Desert. At the north-west of the Caspian Sea, a region of positive causal effect appears over Kazakhstan, linked to the region of positive causal effect in the south, over the Tibetan Plateau. The region of positive causal effect over the Tibetan Plateau further extends to the South China Sea, the Korean peninsula and

325 southern Japan. The SAM influence continues towards the east and shows two regions of positive causal effect (in central North Pacific and central Canada) and one region of negative causal effect over eastern North Pacific.

During El Niño summers, the influence of the SAM is less pronounced in the mid-latitude regions. However, it extends towards the entire tropical Pacific (Fig. 5a).

In the western North Pacific, the most notable feature is the much stronger influence of both the WNPSM and NPH on the

330 North Pacific during El Niño summers (Figs. 5e,f). During those summers, the positive causal effect of the WNPSM over the western North Pacific (Fig. 5e) intensifies with respect to the 1979-2018 causal map (Fig. 4c). Over the western tropical Pacific, in correspondence with the La Niña warm pool, a region of positive causal effect is shown (Fig. 5e). Both features disappear during La Niña summers. Thus, during El Niño summers, the second MCA mode (the WNPSM-NPH pair) shows more intense causal maps whereas during la Niña summers the first MCA mode (SAM-CGT pair) is more important.

335 Calculating MCA pattern during different ENSO phases does not change the results in a qualitative way, although the order of the patterns is reversed in La Niña summers (see Fig. S7, in the Supplementary Material). Moreover, we have checked whether the distribution of the spatial correlation between each MCA mode and the respective Z200/OLR fields changes during different ENSO phases and found that ENSO does not affect the frequency of each pattern in a significant way (see Fig. S8, in the Supplementary Material).

340 As for the 1979-2018 causal maps, when weekly MCA scores obtained from 4-weekly MCA patterns (Fig. S1) are used to provide ENSO-dependent causal maps, consistent results are obtained (see Figs. S9 in the Supplementary Material). Further analysis of possible physical explanations is provided in Section 4.

3.4 MCA causal interactions

345 Finally, we study the role of time-scales on the causal interaction patterns presented above. We create CENs between the two time series of scores for each MCA mode, as identified in Fig. 2 and Fig. S1, and do so for weekly and 4-weekly data for the 1979-2018 period. Figure 6 plots the path coefficient β for two separate sets of CENs built for MCA mode 1 (SAM with CGT, Fig. 6a) and MCA mode 2 (WNPSM with NPH, Fig. 6b) for both 4-weekly and weekly time-scales. As for the causal maps, we use $\tau_{max} = -4$ for weekly data and $\tau_{max} = -1$ for 4-weekly data. In both cases, $\tau_{min} = 0$.

350 At the 4-weekly time-scale, the pair WNPSM-NPH does not show significant causal links (Figs. 6b). The SAM-CGT pair shows two fairly strong causal links with absolute values $\beta \sim 0.3\text{-}0.4$, though with different signs (Figs. 6a). The northward link, i.e. $SAM_{\tau = -1} \rightarrow CGT_{\tau = 0}$, shows a positive $\beta \sim 0.4$: a 1 s.d. shift in the SAM leads to a ~ 0.4 s.d. positive shift in the CGT 4 weeks later (Fig. 6a). The southward link, i.e. $CGT_{\tau = -1} \rightarrow SAM_{\tau = 0}$, shows $\beta \sim -0.3$, meaning that at this time-scale a more intense CGT pattern leads to a weakening of the SAM pattern 4 weeks later (Fig. 6a).

355 At the weekly time-scale, both the $WNPSM_{\tau = -1} \rightarrow NPH_{\tau = 0}$ and the $NPH_{\tau = -1} \rightarrow WNPSM_{\tau = 0}$ links show a $\beta \sim 0.1\text{-}0.2$, indicating that the two-way link has a similar magnitude in both southward and northward directions (Fig. 6b). At this time-scale, the path coefficient β for the $SAM_{\tau = -1} \rightarrow CGT_{\tau = 0}$ link is about a factor 4 smaller than that for the 4-weekly time-scale

(Fig. 6a). The southward link, $CGT_{\tau=-1} \rightarrow SAM_{\tau=0}$, shows a positive $\beta \sim 0.2$ that is about twice as strong as the northward link (Fig. 6a). Thus, the influence of the SAM on the CGT pattern is weak (but present) at shorter (weekly) time-scales, but

360   much stronger at longer (4-weekly) time-scales.

Finally, we tested how the CENs change when the 4-weekly signal is removed from the weekly time series: Each 4-weekly mean is removed from the four values of the corresponding weekly data. This way, we attempt to isolate the dominant time-scales of physical processes behind the different MCA patterns. This is similar in rationale to removing the effects of interannual variability before quantifying intraseasonal variability. Results for the first MCA (SAM and CGT) shows that the

365   path coefficient β for $CGT_{\tau=-1} \rightarrow SAM_{\tau=0}$ link remains almost unaffected (see Fig. S8a, in the Supplementary Material). This suggests that this southward link typically operates at weekly time-scales (rather than 4-weekly), which is rather intuitive since mid-latitude variability dominates at synoptic time-scales. In contrast, the path coefficient β for the northward link ($SAM_{\tau=-1}$ $\rightarrow CGT_{\tau=0}$) becomes insignificant when the 4-weekly signal is removed from the weekly time series, suggesting that the influence from the tropics via the SAM pattern operates at longer, 4-weekly time-scales. Removing the 4-weekly signal from

370   the weekly time series for the second MCA (WNPSM and NPH) roughly halves the path coefficient β for both the northward and southward link (see Fig. S8b in the Supplementary Material).

4 Discussion

In our analysis, we have found that the dominant patterns of interaction between the tropics and mid-latitudes remain qualitatively similar across different sub-seasonal time-scales (weekly and 4-weekly averages) (Fig. 2 and Fig. S1 in the

375   Supplementary Material). Two pairs of co-varying patterns are identified: a) convective activity of the South Asian monsoon (SAM) paired with a mid-latitude wavenumber-5 wave train resembling the circumglobal teleconnection (CGT) pattern and b) convective activity over the western North Pacific, related to the western North Pacific summer monsoon (WNPSM) paired with a second wave-5 circumglobal wave pattern with its strongest action centre represented by the North Pacific High (NPH) and phase shifted with respect to the CGT pattern, to the longitudinal position of WNPSM monsoonal convection in the tropics.

380   These patterns of sub-seasonal co-variability between the mid-latitudes and tropics during boreal summer are remarkably similar to those identified by Ding et al. (2011) for interannual time-scales. This consistency across time-scales (from weekly over monthly to interannual) suggests that the interannual patterns originate from a summation of the same patterns at sub-seasonal time-scales. Still, the strength and sign of the causal interactions are time-scale dependent. At longer time-scales (from monthly to seasonal) slowly varying components such as tropical SST and associated regions of convective activity

385   dominate. Therefore, on these time-scales the causal links from the tropics to mid-latitudes tend to be stronger. At shorter (weekly) time-scales, in general a two-way positive feedback between the tropics and mid-latitudes is found, although strong variability in the mid-latitudes dominates over the tropical convection and thus the reversed southward pathways become stronger. Moreover, we have introduced a novel visualization approach – termed causal maps – that can provide regionally specific information on the causal influence of a specific teleconnection source, and how this signal gets mediated. This way,

390   we identify mid-latitude regions and surface weather conditions that are influenced by tropical drivers. The strongest causal
effect of SAM convection is found over the Saharan region, and depicts the monsoon-desert mechanism (Rodwell and Hoskins,
1996). Also important is the effect of SAM on the central Asian CGT centre of action (see Di Capua et al., 2020). The SAM
also appears to directly influence geopotential heights in the North Pacific and central European surface temperatures one
week ahead. In the North Pacific there is a clear two-way positive influence between the WNPSM and NPH patterns reflecting

395   a Hadley cell-like circulation. This system has a particularly strong influence on central North American and Scandinavian
surface weather conditions (Fig. 4h).

In the tropical belt, the processes behind the identified MCA patterns are linked to strong convection related to the monsoon
activity. Though tropical convection is characterized by heavy precipitation with a typical duration of less than a day, the

400   latent heat release can act as a Rossby wave source for up to two weeks after the initial forcing is removed (Branstator, 2014).
Moreover, while individual convective events are short-lived, the regions of dominant convective activity in the tropics change
on much longer time-scales, such as in response to the BSISO (30-60 days). Thus, this finding could serve as a possible
explanation for why the patterns identified at weekly and 4-weekly time-scales show great similarity (see also the discussion
surrounding Figs. S2 and S3 in the Supplementary Material). It appears reasonable to assume that the tropics operate at longer

405   time-scales providing potential sources of predictability at seasonal-to-subseasonal (S2S) time-scales. In contrast, mid-latitude
circulation in summer is weaker than in winter and is characterized by circumglobal wave trains with typical time-scales of
about one or two weeks (Di Capua et al., 2020; Ding and Wang, 2007; Kornhuber et al., 2016).
On the western North Pacific side, our findings linking the WNPSM convective activity to the NPH, and in turn to a wave-5
circumglobal wave train that affects surface weather condition in the mid-latitudes, further supports previous studies suggesting

410   that convective activity related to this oceanic monsoon system can enhance the high pressure found in the North Pacific mid-
latitudes and that this affects weather conditions in western North America (Chou et al., 2003; Wang et al., 2001). Three centres
of action over European Russia, central North America and the central North Pacific identified in the T2m causal map (Fig.
4h) strongly correspond to the phase locking regions identified for boreal summer wave-5 by Kornhuber et al. (2020), thus
linking the NPH and the WNPSM activity to potential bread-basket failures. Recent evidence indicate that land-atmosphere

415   interactions and increased aridity in mid-latitude regions such as North America and Europe may constitute an enhancing
mechanism for the amplification of circumglobal quasi-stationary Rossby wave events during boreal summer (Teng and
Branstator, 2019). Moreover, the pattern identified in Fig. 5f with a low over central Europe and a high over western Russia,
resembles the results shown by previous studies that link positive geopotential height anomalies over western Russia during
summer 2010 with low-frequency wave trains initiated by La Niña-related convection in the tropical Pacific (Drouard and

420   Woollings, 2018; Hong et al., 2011; Schneidereit et al., 2012; Trenberth and Fasullo, 2012). Therefore, our results support the
importance of the role of Pacific forcing for this wave-5 circumglobal wave pattern. Although other mechanisms could also
be relevant in exciting and maintaining this pattern, the link to the WNPSM convection may hold the potential to affect seasonal
forecasts and climate risks, such as heat waves and simultaneous crop failures.

425 We have applied our causal map analyses to specific ENSO phases to assess the role of El Niño and La Niña in modulating the interactions between mid-latitude circulation and tropical convection in boreal summer. These analyses suggest that in general the ENSO phase does not change the qualitative nature of the causal relationships between different MCA patterns: the signs and strengths of the causal links are largely unaffected (see Fig. 5a-d). Moreover, MCA patterns occur both in La Niña and El Niño summers, and their frequency is hardly affected (Figs. S7-S8). Nevertheless, during La Niña summers, the

430 effect of the SAM-CGT mode is reinforced, while during El Niño summers the WNPSM-NPH pattern dominates. Although, this effect is not very large, it is still important. During La Niña summers, SAM exerts a stronger causal effect on the Tibetan High, along with a reinforced monsoon-desert mechanism and a stronger effect on European circulation. This could be due to the fact that under La Niña conditions, the SAM circulation is supported by a favourable Walker circulation (Ju and Slingo, 1995; Terray et al., 2003). The same applies to the southward link: although ENSO does not alter the normalized causal effect

435 from the CGT to SAM, a stronger CGT pattern in the mid-latitudes would have a stronger absolute effect on SAM activity at the weekly time-scale. At interannual time-scales, Ding et al. (2011) show that the SAM-CGT pair is strongest during the developing phase of ENSO. Therefore, our results further support the hypothesis that ENSO acts on the CGT pattern via its influence on SAM activity, in agreement with Ding et al. (2011). This finding is also in agreement with previous work showing that, at decadal time-scales, the CGT and Silk Road (SRP) patterns intensify under PDO negative (i.e. La Niña-like) forcing

440 (Stephan et al., 2019). During El Niño summers, the SAM shows a more prominent effect on the tropical Pacific. Nevertheless, since we condition on the effect of the CGT, we cannot exclude that this strong signal over the Niño-3.4 region may be due to an element outside our CEN. In the North Pacific, causal maps for different ENSO phases show stronger activity of both WNPSM and NPH links during El Niño summers, consistent with previous literature (Chou et al., 2003; Liu et al., 2016). During El Niño events, tropical convection shifts together with SST anomalies towards the central-eastern Pacific, which may

445 favour WNPSM convective activity. In contrast, during La Niña summers convection is shifted towards the Maritime Continent and the western tropical Indian Ocean, reducing convective activity over the central Pacific and WNPSM region. A weaker WNPSM system may in turn be more prone to the influence of mid-latitude variability on the NPH.

Quantifying the teleconnections between tropics and mid-latitudes is important in order to better understand and constrain

450 future changes in boreal summer circulation. Future projections describe an increase in monsoon precipitation associated with increasing global mean temperature (Menon et al., 2013; Turner and Annamalai, 2012). However, simulations show great uncertainty in the ENSO response to global warming, suggesting an enhanced warming trend in eastern Pacific SST and stronger extreme ENSO events (Cai et al., 2015; Chen et al., 2017a, 2015, 2017b), whereas observations show a La Niña-like warming trend in central-western Pacific SST (Kohyama et al., 2017; Mujumdar et al., 2012). Recent work has shown that this

455 apparent paradox between observations and models might be due to systematic biases in the models in their representation of tropical Pacific SSTs (Seager et al., 2019). Based on our results, if La Niña conditions would become more frequent and SAM activity increases due to global warming, this should favour the influence of the SAM on the CGT pattern and thus on Z200

and T2m patterns across all northern mid-latitudes (Fig. 5f). Finally, a better understating of these teleconnections paves the way for improved S2S forecasts, in particular for the mid-latitude regions, which currently suffer from low seasonal forecasts

460   skill in summer. Our analysis shows that at 4-weekly time-scale, the effect of SAM on the CGT pattern has a path coefficient β ~ 0.4, thus indicating potential for predictability. Further work should analyse how the causal links between these teleconnection patterns are reproduced in corresponding state-of-the-art S2S forecast and climate models, respectively.

Finally, it should not be forgotten that in the context of the present work, the term *causal* rests upon several assumptions, such

465   as the causal Markov condition, faithfulness, causal sufficiency, stationarity of the causal links and the assumptions made on the dependence-type (Runge, 2018). These assumptions can be violated in a real system and it is important to be aware of the associated typical challenges for causal discovery in Earth system sciences (Runge et al., 2019). Causal sufficiency requires that all the important actors in a specific system are accounted for. Here, given the limited set of actors analysed, it cannot be excluded that other not-included actors may act as important (common) drivers. Therefore, the obtained links can be considered

470   *causal* only with respect to the specific set of actors used here. However, the *absence* of a link can still be interpreted as a likely indication that no direct physical connection among the respective variables exists. Moreover, we assume linear dependencies and stationarity for the detection of the causal links. While linearity has been shown to be a useful assumption in previous work (Di Capua et al., 2020), monsoon dynamics behaves partly nonlinearly and therefore, our causal networks by construction only capture some part of the underlying mechanisms. Also, the SAM teleconnections might well behave in an

475   nonstationary manner on decadal time-scales (Di Capua et al., 2019; Robock et al., 2003). We therefore cannot rule out that decadal and interdecadal oscillations such as the Pacific Decadal Oscillation may influence our results. However, the amount of reliable data is limited and this prohibits the application of nonlinear measures or to study effects due to nonstationarity.

480   **5 Conclusions**

We have analysed the interdependencies and spatial effects of the two main MCA modes of co-variability between tropical convection and Northern Hemisphere mid-latitude circulation in boreal summer. The first MCA pair connects the circumglobal teleconnection (CGT) pattern in the mid-latitudes with the South Asian monsoon (SAM) convection, while the second MCA pair connects the western North Pacific summer monsoon (WNPSM) convection with a second circumglobal pattern related

485   to the North Pacific High (NPH). These patterns appear qualitatively independent of the analysed time-scales and emerge in weekly, 4-weekly and interannual analyses. The strength of the causal links *is* time-scale dependent. In particular, the influence of SAM on CGT is strongest at 4-weekly time-scale, while the reversed link is stronger at weekly time-scale. The patterns and sign of the standardized causal effect links are also not strongly affected by ENSO. Still, during La Niña years the effect of the

SAM on the mid-latitudes intensifies while during El Niño years the WNPSM effect on the mid-latitudes dominates. Moreover,
490   the boreal summer intraseasonal oscillation exerts strong control on the SAM convection at various lags.

Furthermore, we have introduced causal maps, a new application of the concept of causal effect networks and have highlighted
how this method can overcome limitations of correlation maps by removing spurious links. These causal maps further confirm
our findings by showing a general positive two-way causal relationship between the dominant modes. Moreover, they highlight
specific regions in the mid-latitudes that are particularly affected by the tropical modes (e.g. Eurasia, North America). These
495   findings provide an improved understanding of the interactions between tropical convective activity and circumglobal wave
trains that characterize mid-latitude circulation in boreal summer. This paves the way for improving sub-seasonal forecasts as
well as constraining future projections of boreal summer circulation. Further work shall assess whether these causal
relationships are captured by general circulation models and whether this knowledge can be used to improve seasonal forecasts
over the mid-latitudes.

500

References

Benjamini, Y. and Hochberg, Y.: Controlling the False Discovery Rate: a Practical and Powerful Approach to Multiple Testing,
J. R. Stat. Soc. Ser. B, 57(1), 289–300, doi:10.2307/2346101, 1995.

Beverley, J. D., Woolnough, S. J., Baker, L. H., Johnson, S. J. and Weisheimer, A.: The northern hemisphere circumglobal
505   teleconnection in a seasonal forecast model and its relationship to European summer forecast skill, Clim. Dyn., 52(5–6), 3759–
3771, doi:10.1007/s00382-018-4371-4, 2019.

Branstator, G.: Long-lived response of the midlatitude circulation and storm tracks to pulses of tropical heating, J. Clim.,
27(23), 8809–8826, doi:10.1175/JCLI-D-14-00312.1, 2014.

Branstator, G. W.: Circumglobal teleconnections, the jet stream waveguide, and the North Atlantic Oscillation, J. Clim., 15,
510   1893–1910, doi:10.1175/1520-0442(2002)015<1893:CTTJSW>2.0.CO;2, 2002.

Briegel, L. M. and Frank, W. M.: Large-scale influences on tropical cyclogenesis in the western North Pacific, Mon. Weather
Rev., 125(7), 1397–1413, doi:10.1175/1520-0493(1997)125<1397:LSIOTC>2.0.CO;2, 1997.

Cai, W., Santoso, A., Wang, G., Yeh, S. W., An, S. Il, Cobb, K. M., Collins, M., Guilyardi, E., Jin, F. F., Kug, J. S., Lengaigne,
M., Mcphaden, M. J., Takahashi, K., Timmermann, A., Vecchi, G., Watanabe, M. and Wu, L.: ENSO and greenhouse warming,
515   Nat. Clim. Chang., 5(9), 849–859, doi:10.1038/nclimate2743, 2015.

Di Capua, G., Kretschmer, M., Runge, J., Alessandri, A., Donner, R. V., van den Hurk, B., Vellore, R., Krishnan, R. and
Coumou, D.: Long-Lead Statistical Forecasts of the Indian Summer Monsoon Rainfall Based on Causal Precursors, Weather
Forecast., 34(5), 1377–1394, doi:10.1175/waf-d-19-0002.1, 2019.

Di Capua, G., Kretschmer, M., Donner, R. V., Van Den Hurk, B., Vellore, R., Krishnan, R. and Coumou, D.: Tropical and
520   mid-latitude teleconnections interacting with the Indian summer monsoon rainfall: A theory-guided causal effect network

approach, Earth Syst. Dyn., 11(1), 17–34, doi:10.5194/esd-11-17-2020, 2020.

Chakraborty, A. and Krishnamurti, T. N.: A coupled model study on ENSO, MJO and Indian summer monsoon rainfall relationships, Meteorol. Atmos. Phys., 84(3–4), 243–254, doi:10.1007/s00703-002-0601-7, 2003.

Chen, C., Cane, M. A., Wittenberg, A. T. and Chen, D.: ENSO in the CMIP5 Simulations: Life Cycles, Diversity, and
525 Responses to Climate Change, J. Clim., 30(2), 775–801, doi:10.1175/jcli-d-15-0901.1, 2017a.

Chen, L., Li, T. and Yu, Y.: Causes of strengthening and weakening of ENSO amplitude under global warming in four CMIP5 models, J. Clim., 28(8), 3250–3274, doi:10.1175/JCLI-D-14-00439.1, 2015.

Chen, L., Li, T., Yu, Y. and Behera, S. K.: A possible explanation for the divergent projection of ENSO amplitude change under global warming, Clim. Dyn., 49(11–12), 3799–3811, doi:10.1007/s00382-017-3544-x, 2017b.

530 Cherchi, A., Annamalai, H., Masina, S. and Navarra, A.: South Asian summer monsoon and the eastern Mediterranean climate: The monsoon-desert mechanism in CMIP5 simulations, J. Clim., 27(18), 6877–6903, doi:10.1175/JCLI-D-13-00530.1, 2014.

Chou, C., Tu, J. Y. and Yu, J. Y.: Interannual variability of the Western North Pacific summer monsoon: Differences between ENSO and non-ENSO years, J. Clim., 16(13), 2275–2287, doi:10.1175/2761.1, 2003.

Choudhury, A. D. and Krishnan, R.: Dynamical Response of the South Asian Monsoon Trough to Latent Heating from
535 Stratiform and Convective Precipitation, J. Atmos. Sci., 68(6), 1347–1363, doi:10.1175/2011JAS3705.1, 2011.

Dee, D. P., Uppala, S. M., Simmons, a. J., Berrisford, P., Poli, P., Kobayashi, S., Andrae, U., Balmaseda, M. a., Balsamo, G., Bauer, P., Bechtold, P., Beljaars, a. C. M., van de Berg, L., Bidlot, J., Bormann, N., Delsol, C., Dragani, R., Fuentes, M., Geer, a. J., Haimberger, L., Healy, S. B., Hersbach, H., Hólm, E. V., Isaksen, L., Kållberg, P., Köhler, M., Matricardi, M., Mcnally, a. P., Monge-Sanz, B. M., Morcrette, J. J., Park, B. K., Peubey, C., de Rosnay, P., Tavolato, C., Thépaut, J. N. and
540 Vitart, F.: The ERA-Interim reanalysis: Configuration and performance of the data assimilation system, Q. J. R. Meteorol. Soc., 137(656), 553–597, doi:10.1002/qj.828, 2011.

Ding, Q. and Wang, B.: Circumglobal teleconnection in the Northern Hemisphere summer, J. Clim., 18(17), 3483–3505, doi:10.1175/JCLI3473.1, 2005.

Ding, Q. and Wang, B.: Intraseasonal teleconnection between the summer Eurasian wave train and the Indian Monsoon, J.
545 Clim., 20(15), 3751–3767, doi:10.1175/JCLI4221.1, 2007.

Ding, Q., Wang, B., Wallace, J. M. and Branstator, G.: Tropical-extratropical teleconnections in boreal summer: Observed interannual variability, J. Clim., 24(7), 1878–1896, doi:10.1175/2011JCLI3621.1, 2011.

Drouard, M. and Woollings, T.: Contrasting Mechanisms of Summer Blocking Over Western Eurasia, Geophys. Res. Lett., 45(21), 12,040-12,048, doi:10.1029/2018GL079894, 2018.

550 Gadgil, S. and Joseph, P. V: On breaks of the Indian monsoon, Proc. Indian Acad. Sci. (Earth Planet. Sci.), 112(4), 529–558, doi:https://doi.org/10.1007/BF02709778, 2003.

Goswami, B. N. and Ajaya Mohan, R. S.: Intraseasonal Oscillations and Interannual Variability of the Indian Summer Monsoon, J. Clim., 14, 1180–1198, doi:10.1007/BF02842260, 2001.

Goswami, B. N., Sengupta, D. and Suresh Kumar, G.: Intraseasonal oscillations and interannual variability of surface winds

555   over the Indian monsoon region, Proc. Indian Acad. Sci. Earth Planet. Sci., 107(1), 45–64, doi:10.1007/BF02842260, 1998.

Hong, C. C., Hsu, H. H., Lin, N. H. and Chiu, H.: Roles of European blocking and tropical-extratropical interaction in the 2010 Pakistan flooding, Geophys. Res. Lett., 38(13), 1–6, doi:10.1029/2011GL047583, 2011.

Joseph, S., Sahai, A. K., Chattopadhyay, R. and Goswami, B. N.: Can El Niño-Southern Oscillation (ENSO) events modulate intraseasonal oscillations of Indian summer monsoon?, J. Geophys. Res. Atmos., 116(20), 1–12, doi:10.1029/2010JD015510,
560   2011.

Ju, J. and Slingo, J.: The Asian summer monsoon and ENSO, Q. J. R. Meteorol. Soc., 121, 1133–1168, doi:10.1002/j.1477-8696.1997.tb06267.x, 1995.

Kang, I. S., Ho, C. H., Lim, Y. K. and Lau, K. M.: Principal modes of climatological seasonal and intraseasonal variations of the Asian summer monsoon, Mon. Weather Rev., 127(2–3), 322–340, doi:10.1175/1520-
565   0493(1999)127<0322:pmocsa>2.0.co;2, 1999.

Kikuchi, K. and Wang, B.: Formation of tropical cyclones in the Northern Indian ocean associated with two types of tropical intraseasonal oscillation modes, J. Meteorol. Soc. Japan, 88(3), 475–496, doi:10.2151/jmsj.2010-313, 2010.

Kikuchi, K., Wang, B. and Kajikawa, Y.: Bimodal representation of the tropical intraseasonal oscillation, Clim. Dyn., 38(9–10), 1989–2000, doi:10.1007/s00382-011-1159-1, 2012.

570   Kohyama, T., Hartmann, D. L. and Battisti, D. S.: La Niña-like mean-state response to global warming and potential oceanic roles, J. Clim., 30(11), 4207–4225, doi:10.1175/JCLI-D-16-0441.1, 2017.

Kornhuber, K., Petoukhov, V., Petri, S., Rahmstorf, S. and Coumou, D.: Evidence for wave resonance as a key mechanism for generating high-amplitude quasi-stationary waves in boreal summer, Clim. Dyn., 49(5–6), 1961–1979, doi:10.1007/s00382-016-3399-6, 2016.

575   Kornhuber, K., Coumou, D., Vogel, E., Lesk, C., Donges, J. F., Lehmann, J. and Horton, R. M.: Amplified Rossby waves enhance risk of concurrent heatwaves in major breadbasket regions, Nat. Clim. Chang., 20, 48–53, doi:10.1038/s41558-019-0637-z, 2020.

Kretschmer, M., Coumou, D., Donges, J. F. and Runge, J.: Using Causal Effect Networks to analyze different Arctic drivers of mid-latitude winter circulation, J. Clim., 29, 4069–4081, doi:10.1175/JCLI-D-15-0654.1, 2016.

580   Kretschmer, M., Cohen, J., Matthias, V., Runge, J. and Coumou, D.: The different stratospheric influence on cold-extremes in Eurasia and North America, npj Clim. Atmos. Sci., 1(1), 1–10, doi:10.1038/s41612-018-0054-4, 2018.

Kripalani, R. H. Ã., Kulkarni, A. and Singh, S. V.: Association of the Indian summer monsoon with the northern hemisphere mid-latitude circulation, Int. J. Climatol., 17(10), 1055–1067, doi:https://doi.org/10.1002/(SICI)1097-0088(199708)17:10<1055::AID-JOC180>3.0.CO;2-3, 1997.

585   Krishna Kumar, K., Rajagopalan, B. and Cane, M.: On the weakening relationship between the indian monsoon and ENSO, Science, 284(5423), 2156–2159, doi:DOI 10.1126/science.284.5423.2156, 1999.

Krishna Kumar, K., Rajagopalan, B., Hoerling, M., Bates, G. and Cane, M.: Unraveling the Mystery of Indian Monsoon Failure During El Nino, Science (80-.)., 314(October), 115–119, doi:10.1126/science.1131152, 2006.

Krishnamurti, T. N. and Surgi, N.: Observational aspects of the summer monsoon, in Monsoon Meteorology, edited by C.-P. Chang and T. N. Krishnamurti, pp. 3–25, Oxford University Press., 1987.

Krishnan, R., Zhang, C. and Sugi, M.: Dynamics of Breaks in the Indian Summer Monsoon, J. Atmos. Sci., 57(1969), 1354–1372, 2000.

Lau, W. K. M. and Kim, K.-M.: The 2010 Pakistan Flood and Russian Heat Wave : Teleconnection of Hydrometeorological Extremes, J. Hydrometeorol., 13, 392–403, doi:10.1175/JHM-D-11-016.1, 2011.

Li, T. and Wang, B.: A review on the western North Pacific monsoon: Synoptic-to-interannual variabilities, Terr. Atmos. Ocean. Sci., 16(2), 285–314, doi:10.3319/TAO.2005.16.2.285(A), 2005.

Liu, F., Li, T., Wang, H., Deng, L. and Zhang, Y.: Modulation of boreal summer intraseasonal oscillations over the Western North Pacific by ENSO, J. Clim., 29(20), 7189–7201, doi:10.1175/JCLI-D-15-0831.1, 2016.

Lu, R.: Interannual variability of the summertime North Pacific subtropical high and its relation to atmospheric convection over the warm pool, J. Meteorol. Soc. Japan, 79(3), 771–783, doi:10.2151/jmsj.79.771, 2001.

McGraw, M. C. and Barnes, E. A.: Memory matters: A case for granger causality in climate variability studies, J. Clim., 31(8), 3289–3300, doi:10.1175/JCLI-D-17-0334.1, 2018.

Menon, A., Levermann, A., Schewe, J., Lehmann, J. and Frieler, K.: Consistent increase in Indian monsoon rainfall and its variability across CMIP-5 models, Earth Syst. Dyn., 4(2), 287–300, doi:10.5194/esd-4-287-2013, 2013.

Mujumdar, M., Preethi, B., Sabin, T. P., Ashok, K., Saeed, S., Pai, D. S. and Krishnan, R.: The Asian summer monsoon response to the La Niña event of 2010, Meteorol. Appl., 19(2), 216–225, doi:10.1002/met.1301, 2012.

Nitta, T.: Convective Activities in the Tropical Western Pacific and Their Impact on the Northern Hemisphere Summer Circulation, J. Meteorol. Soc. Japan, 65(3), 373–390, 1987.

O'Reilly, C. H., Woollings, T., Zanna, L. and Weisheimer, A.: The impact of tropical precipitation on summertime euro-Atlantic circulation via a circumglobal wave train, J. Clim., 31(16), 6481–6504, doi:10.1175/JCLI-D-17-0451.1, 2018.

O'Reilly, C. H., Woollings, T., Zanna, L. and Weisheimer, A.: An interdecadal shift of the extratropical teleconnection from the tropical Pacific during boreal summer, Geophys. Res. Lett., doi:10.1029/2019gl084079, 2019.

Rao, Y. P. P.: Southwest monsoon, METEOROLOG., Meteorological Monograph: Synoptic Meteorology., 1976.

Riyu, L.: Indices of the Summertime Western North Pacific Subtropical High, Adv. Atmos. Sci., 19(6), doi:10.1007/s00376-002-0061-5, 2002.

Robock, A., Mu, M., Vinnikov, K. and Robinson, D.: Land Surface Conditions over Eurasia and Indian summer monsoon rainfall, J. Geophys. Res., 108(D4), 1–17, doi:10.1029/2002JD002286, 2003.

Rodwell, M. J. and Hoskins, B.: Monsoons and the dynamics of deserts, Q. J. R. Meteorol. Soc., 122, 1385–1404, 1996.

Runge, J.: Causal network reconstruction from time series : From theoretical assumptions to practical estimation, Chaos, 28, 075310, doi:10.1063/1.5025050, 2018.

Runge, J., Petoukhov, V. and Kurths, J.: Quantifying the strength and delay of climatic interactions: The ambiguities of cross correlation and a novel measure based on graphical models, J. Clim., 27(2), 720–739, doi:10.1175/JCLI-D-13-00159.1, 2014.

Runge, J., Petoukhov, V., Donges, J. F., Hlinka, J., Jajcay, N., Vejmelka, M., Hartman, D., Marwan, N., Paluš, M. and Kurths, J.: Identifying causal gateways and mediators in complex spatio-temporal systems, Nat. Commun., 6, 9502, doi:10.1038/ncomms9502, 2015a.

Runge, J., Donner, R. V. and Kurths, J.: Optimal model-free prediction from multivariate time series, Phys. Rev. E - Stat. Nonlinear, Soft Matter Phys., 91(5), 052909, doi:10.1103/PhysRevE.91.052909, 2015b.

Runge, J., Nowack, P., Kretschmer, M., Flaxman, S. and Sejdinovic, D.: Detecting causal associations in large nonlinear time series datasets, Sci. Adv., 5, eaau4996, 2019.

Saha, S. K., Halder, S., Suryachandra Rao, A. and Goswami, B. N.: Modulation of ISOs by land-atmosphere feedback and contribution to the interannual variability of Indian summer monsoon, J. Geophys. Res. Atmos., 117(13), 1–14, doi:10.1029/2011JD017291, 2012.

Schneidereit, A., Schubert, S., Vargin, P., Lunkeit, F., Zhu, X., Peters, D. H. W. and Fraedrich, K.: Large-scale flow and the long-lasting blocking high over Russia: Summer 2010, Mon. Weather Rev., 140(9), 2967–2981, doi:10.1175/MWR-D-11-00249.1, 2012.

Schubert, S., Wang, H. and Suarez, M.: Warm season subseasonal variability and climate extremes in the northern hemisphere: The role of stationary Rossby waves, J. Clim., 24(18), 4773–4792, doi:10.1175/JCLI-D-10-05035.1, 2011.

Seager, R., Cane, M., Henderson, N., Lee, D. E., Abernathey, R. and Zhang, H.: Strengthening tropical Pacific zonal sea surface temperature gradient consistent with rising greenhouse gases, Nat. Clim. Chang., 9(7), 517–522, doi:10.1038/s41558-019-0505-x, 2019.

Spirtes, P., Glymour, C. and Scheines, R.: Causation, prediction, and search, Boston: The MIT Press., 2000.

Srivastava, A., Pradhan, M., Goswami, B. N. and Rao, S. A.: Regime shift of Indian summer monsoon rainfall to a persistent arid state: external forcing versus internal variability, Meteorol. Atmos. Phys., (0123456789), 1–14, doi:10.1007/s00703-017-0565-2, 2017.

Stephan, C. C., Klingaman, N. P. and Turner, A. G.: A mechanism for the interdecadal variability of the Silk Road Pattern, J. Clim., 32, 717–736, doi:10.1175/JCLI-D-18-0405.1, 2019.

Suhas, E., Neena, J. M. and Goswami, B. N.: Interannual Variability of Indian Summer Monsoon arising from Interactions between Seasonal Mean and Intraseasonal Oscillations, J. Atmos. Sci., 69(6), 1761–1774, doi:10.1175/JAS-D-11-0211.1, 2012.

Teng, H. and Branstator, G.: Amplification of Waveguide Teleconnections in the Boreal Summer, Curr. Clim. Chang. Reports, 5(4), 421–432, doi:10.1007/s40641-019-00150-x, 2019.

Terray, P., Delecluse, P., Labattu, S. and Terray, L.: Sea surface temperature associations with the late Indian summer monsoon, Clim. Dyn., 21(7–8), 593–618, doi:10.1007/s00382-003-0354-0, 2003.

Thomson, S. I. and Vallis, G. K.: Atmospheric response to SST anomalies. Part II: Background-state dependence, teleconnections, and local effects in summer, J. Atmos. Sci., 75(12), 4125–4138, doi:10.1175/JAS-D-17-0298.1, 2018.

Trenberth, K. E. and Fasullo, J. T.: Climate extremes and climate change: The Russian heat wave and other climate extremes

of 2010, J. Geophys. Res. Atmos., 117(July), n/a-n/a, doi:10.1029/2012JD018020, 2012.

Turner, A. G. and Annamalai, H.: Climate change and the south Asian summer monsoon, Nat. Clim. Chang., 2(June), doi:10.1038/NCLIMATE1495, 2012.

660   Vellore, R. K., Krishnan, R., Pendharkar, J., Choudhury, A. D. and Sabin, T. P.: On the anomalous precipitation enhancement over the Himalayan foothills during monsoon breaks, Clim. Dyn., 43(7–8), 2009–2031, doi:10.1007/s00382-013-2024-1, 2014.

Vellore, R. K., Kaplan, M. L., John, R. K., Sabade, S., Deshpande, N. and Singh, B. B.: Monsoon - extratropical circulation interactions in Himalayan extreme rainfall, Clim. Dyn., 46(11), 3517–3546, doi:10.1007/s00382-015-2784-x, 2016.

665   Wang, B. and Xu, X.: Northern Hemisphere summer monsoon singularities and climatological intraseasonal oscillation, J. Clim., 10(5), 1071–1085, doi:10.1175/1520-0442(1997)010<1071:NHSMSA>2.0.CO;2, 1997.

Wang, B., Wu, R. and Lau, K. M.: Interannual variability of the asian summer monsoon: Contrasts between the Indian and the Western North Pacific-East Asian monsoons, J. Clim., 14(20), 4073–4090, doi:10.1175/1520-0442(2001)014<4073:IVOTAS>2.0.CO;2, 2001.

670   Weisheimer, A. and Palmer, T. N.: On the reliability of seasonal climate forecasts, J. R. Soc. Interface, 11(96), 20131162, doi:10.1098/rsif.2013.1162, 2014.

Wiedermann, M., Donges, J. F., Handorf, D., Kurths, J. and Donner, R. V.: Hierarchical structures in Northern Hemispheric extratropical winter ocean–atmosphere interactions, Int. J. Climatol., 37(10), 3821–3836, doi:10.1002/joc.4956, 2017.

Wilks, D. S.: Canonical Correlation Analysis (CCA), Int. Geophys., 100(1992), 563–582, doi:10.1016/B978-0-12-385022-

675   5.00013-0, 2011.

Wu, R., Chen, J. and Chen, W.: Different types of ENSO influences on the Indian summer monsoon variability, J. Clim., 25(3), 903–920, doi:10.1175/JCLI-D-11-00039.1, 2012.

Xavier, P. K., Marzin, C. and Goswami, B. N.: An objective definition of the Indian summer monsoon season and a new perspective on the ENSO–monsoon relationship Prince, R. Meteorol. Soc., 133, 749–764, doi:10.1002/qj, 2007.

680   Yim, S. Y., Yeh, S. W., Wu, R. and Jhun, J. G.: The influence of ENSO on decadal variations in the relationship between the East Asian and western North Pacific summer monsoons, J. Clim., 21(13), 3165–3179, doi:10.1175/2007JCLI1948.1, 2008.

685
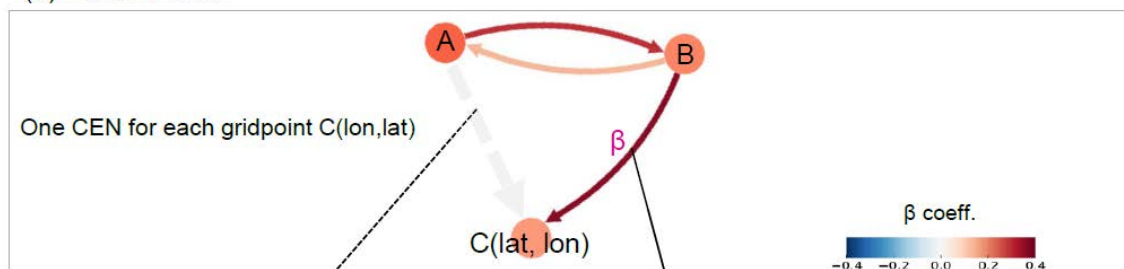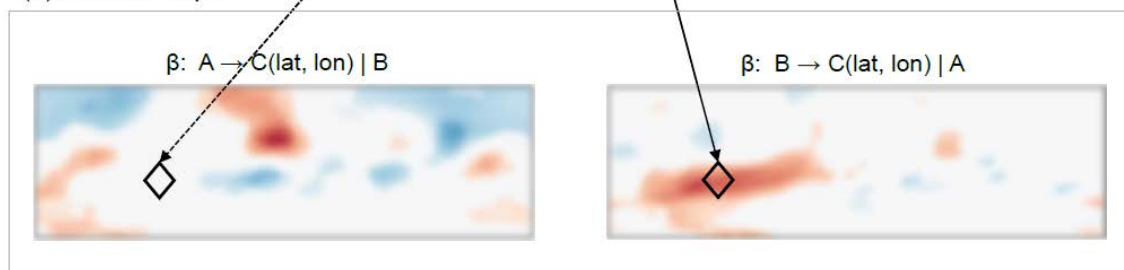
Figure 1: Schematic explanation of causal maps. Panel (a) shows the correlation maps for *A* with *C*(lat, lon) (left panel) and *B* with *C*(lat, lon) (right panel). Panel (b) shows an example of a CEN constructed with *A*, *B* and *C*(lat, lon) for a specific geographical position (identified with a diamond in the 2D maps). Panel (c) shows the corresponding causal maps showing the path coefficients *β* from *A* to *C*, conditioned on *B* and all autocorrelations (bottom-left panel) and from *B* to *C*, conditioned on *A* and all autocorrelations (bottom-right panel). The "|" denotes the conditioned-out actor: *A* for the right panel and *B* for the left panel. See text for further description.

690
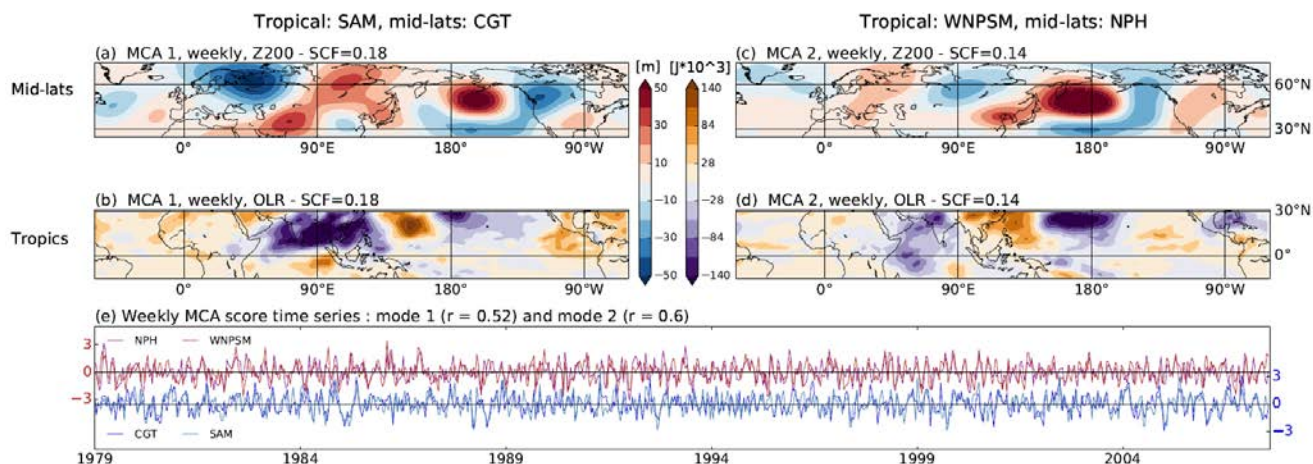
Figure 2: MCA of mid-latitude Z200 and tropical OLR at intraseasonal time-scales. Panels (a) and (b) show the first MCA mode for mid-latitude Z200 (25-75° N) and tropical OLR (15°S-30°N), respectively, at the weekly time-scale. The first MCA highlights the circumglobal teleconnection (CGT) pattern in the mid-latitudes and the South Asian monsoon (SAM) in the tropical belt. Panels (c) and (d): Same as for panel (a) and (b) but for the second MCA mode. This mode depicts the North Pacific High (NPH) in the mid-latitudes and the western North Pacific summer monsoon (WNPSM) in the tropical belt. The squared covariance fraction (SCF) of each MCA mode is given on top of the panels. Panel (e) shows the time series of MCA scores for the two MCA modes at weekly time-scale. Each MCA pattern has its own time series, i.e. one for tropical OLR and one for mid-latitude Z200 (note that different y-axes are used).
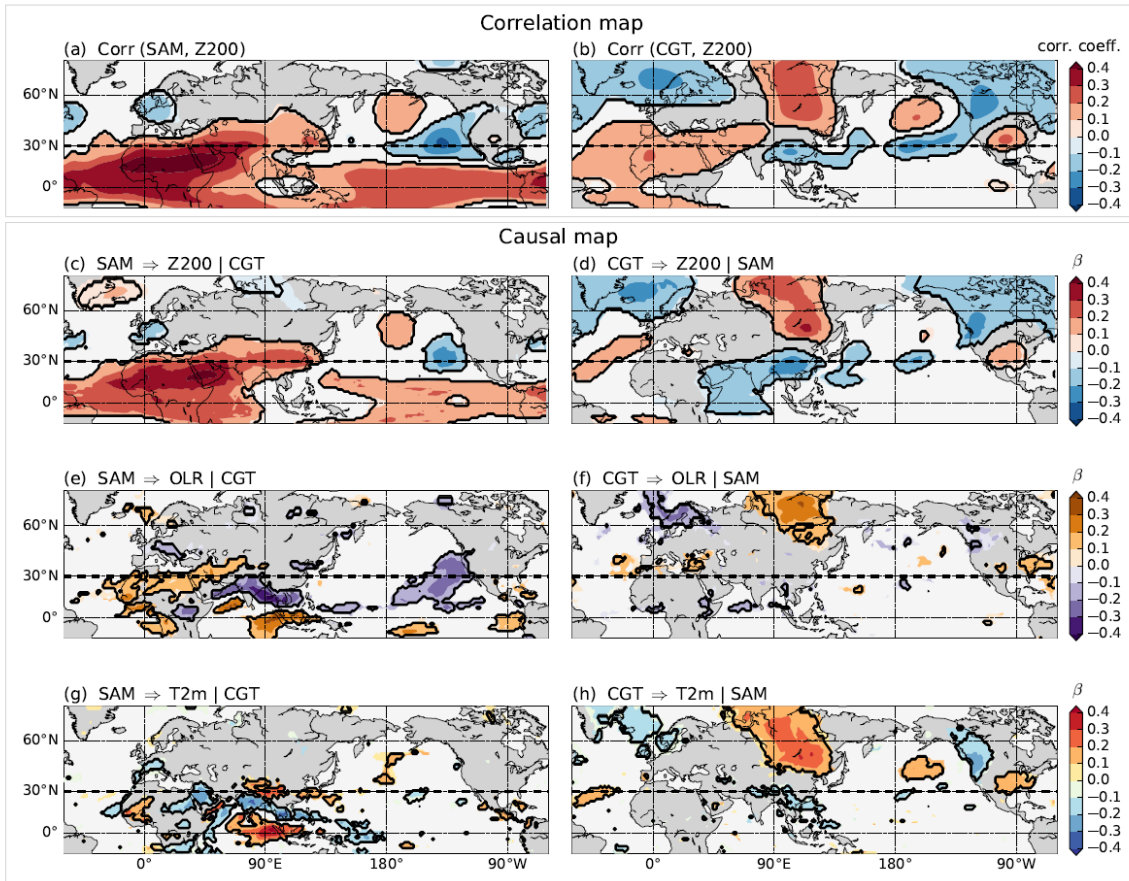
Figure 3: Influence of MCA mode 1 on Northern Hemisphere circulation. Panel (a): correlation map between the weekly SAM time series and the Z200 field. Panel (b): Same as panel (a) but for the correlation between weekly CGT time series and the Z200 field. Panel (c): path coefficient β for link $SAM_{\tau=-1} \rightarrow Z200_{\tau=0}$ for a 3-actors CEN built with SAM, CGT and Z200. Here, the "|" denotes the conditioned-out actor: CGT. Panel (d): Same as panel (c) but for the link $CGT_{\tau=-1} \rightarrow Z200_{\tau=0}$. The "|" denotes the conditioned-out actor: SAM. Panels (e) and (g): Same as panel (c) but for the influence of SAM on OLR and T2m fields respectively. Panels (f) and (h): Same as panel (d) but for the influence of CGT on OLR and T2m fields respectively. Only path coefficients β with $p < 0.05$ (accounting for the effect of serial correlations) are shown by black contours, while grid points which are found significant only with non-corrected p-values are shaded. The dashed black line located at 30°N shows the border between the tropical and the mid-latitude belt which separates OLR and Z200 analysis.
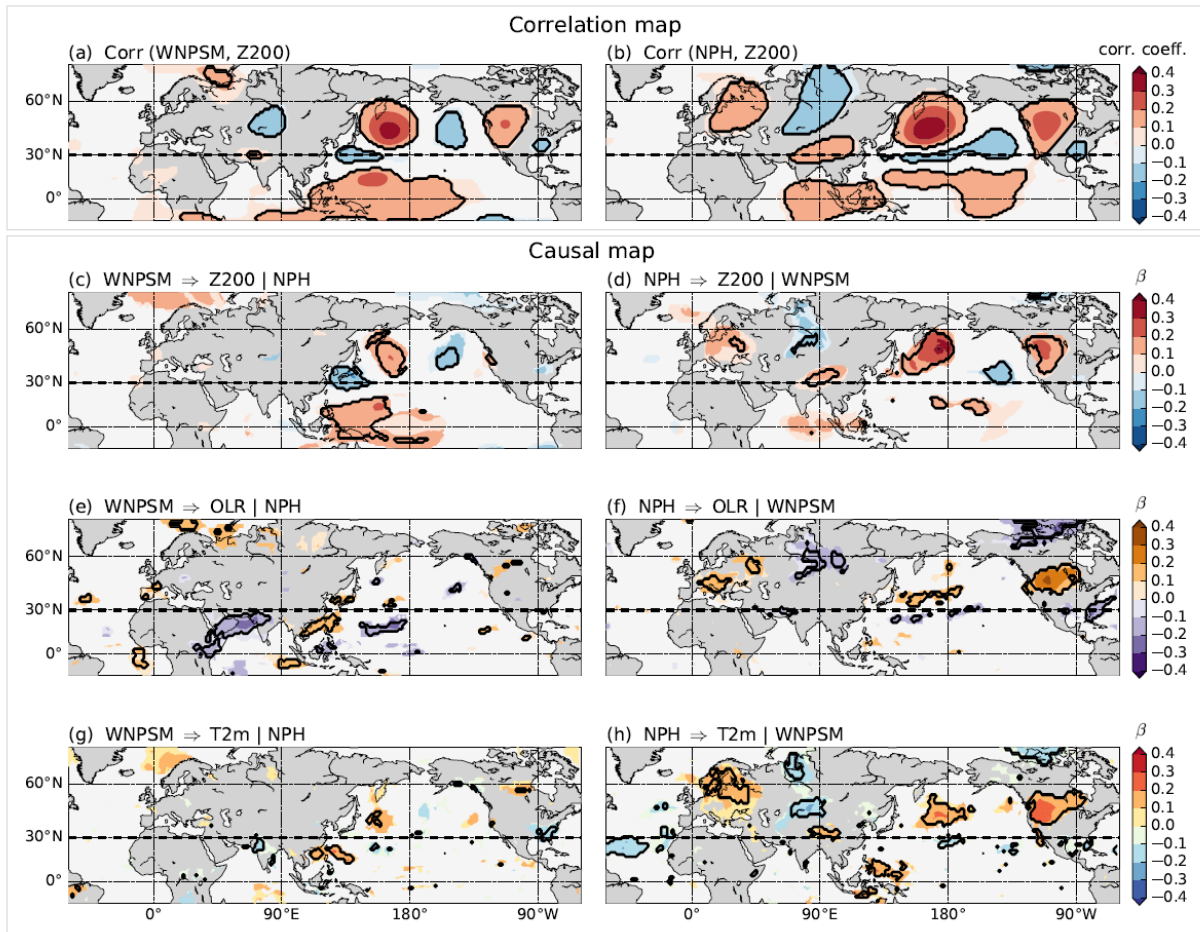
Figure 4: Influence of MCA mode 2 on Northern Hemisphere circulation. Panel (a): correlation between the weekly WNPSM time series and the Z200 field. Panel (b): Same as panel (a) but for the correlation between weekly NPH time series and the Z200 field. Panel (c): path coefficient β for the link WNPSM $_{\tau=-1} \to$ Z200$_{\tau=0}$ in a 3-actors CEN built with WNPSM, NPH and Z200. Here, the "|" denotes the conditioned-out actor: NPH. Panel (d): Same as panel (c) but for the link NPH $_{\tau=-1} \to$ Z200$_{\tau=0}$. Here, the "|" denotes the conditioned-out actor: WNPSM. Panels (e) and (g): Same as panel (c) but for the influence of WNPSM on OLR and T2m fields respectively. Panels (f) and (h): Same as panel (d) but for the influence of NPH on OLR and T2m fields respectively. Only path coefficients β with $p < 0.05$ (accounting for the effect of serial correlations) are shown by black contours, while grid points which are found significant only with non-corrected p-values are shaded. The dashed black line located at 30°N shows the border between the tropical and the mid-latitude belt which separates OLR and Z200 analysis.
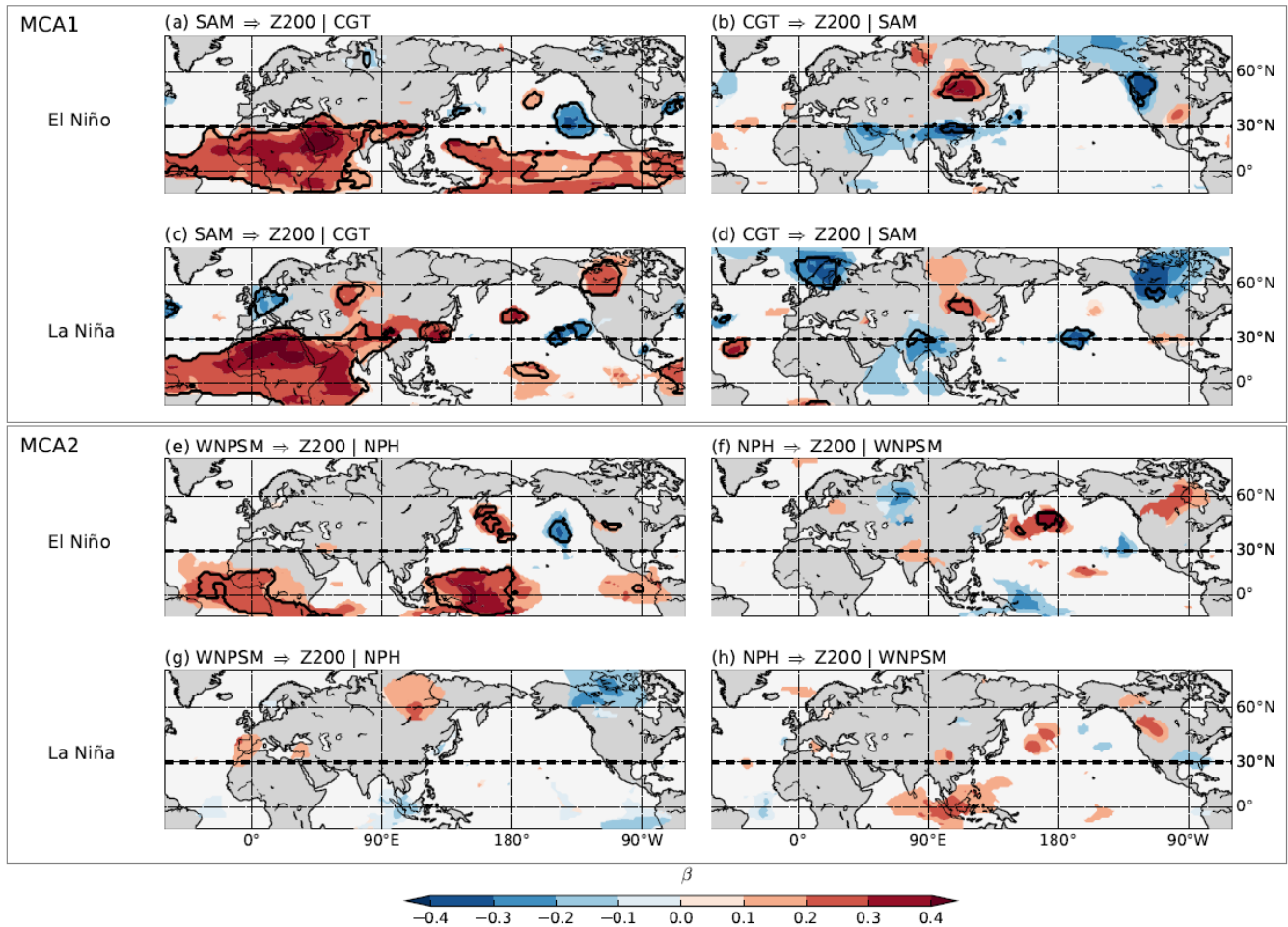
Figure 5: Causal maps and ENSO influence. Panel (a) shows the β for link SAM$_{\tau=-1} \rightarrow$ Z200$_{\tau=0}$ a 3-actors CEN built with SAM, CGT and Z200 during El Niño years. Here, the "|" denotes the conditioned-out actor: CGT. Panel (b) and (d): Same as panels (a) and (c) but for the link CGT$_{\tau=-1} \rightarrow$ Z200$_{\tau=0}$. The "|" denotes the conditioned-out actor: SAM. Panel (c): Same as panel (a) but for La Niña years. Panel (e) and (g): Same as panels (a) and (c) but for the link WNPSM$_{\tau=-1} \rightarrow$ Z200$_{\tau=0}$ from a 3-actors CEN built with WNPSM, NPH and Z200. Panel (f) and (h): Same as panels (e) and (g) but for the link NPH$_{\tau=-1} \rightarrow$ Z200$_{\tau=0}$. Only path coefficients β with $p < 0.05$ (accounting for the effect of serial correlations) are shown by black contours, while grid points which are found significant only with non-corrected p-values are shaded. The dashed black line located at 30°N shows the border between the tropical and the mid-latitude belt which separates OLR and Z200 analysis.
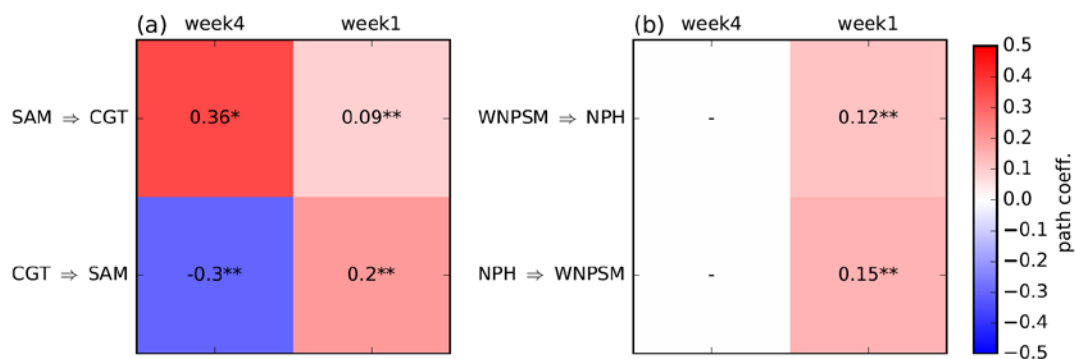
735 **Figure 6: Two-way link between tropical OLR and mid-latitude Z200.** Shown is the path coefficient for pairs of MCA time series. The CGT is studied along with the SAM, while the NPH is analysed together with the WNPSM. Panel (a) shows the path coefficient β for the link SAM $_{\tau=-1}$ → CGT $_{\tau=0}$ over the 1979-2018 period (first row), and path coefficient β for the link CGT $_{\tau=-1}$ → SAM $_{\tau=0}$ (second row). 4-weekly β are shown in the left column, weekly β values are shown in the right column. Panel (b): Same as for panel (a) but for WNPSM $_{\tau=-1}$ → NPH $_{\tau=0}$ and NPH $_{\tau=-1}$ → WNPSM $_{\tau=0}$ links respectively. β values with $p < 0.1$ (0.05) are identified with one (two) asterisks.

740

745

Acknowledgments

This work has been financially supported by the German Federal Ministry for Education and Research of Germany (BMBF) via the Belmont Forum / JPI Climate project GOTHAM (grant no. 01LP1611A) and the BMBF Young Investigators Group CoSy-CC^2: Complex Systems Approaches to Understanding Causes and Consequences of Past, Present and Future Climate
750 Change (grant no. 01LN1306A). The contribution of AGT was supported by NERC in the UK under the BITMAP project (grant number NE/P006795/1) and in the STIMULATE project through the Weather and Climate Science for Service Partnership (WCSSP) India, a collaborative initiative between the Met Office, supported by the UK Government's Newton Fund, and the Indian Ministry of Earth Sciences (MoES).

755 **Data availability.** The data used in this article can be accessed by contacting the corresponding author.

Author contributions. GDC, DC, BvdH, JR and AGT designed the analysis. GDC performed the analysis and wrote the first draft of the paper. All authors contributed to the interpretation of the results and to the writing of the paper.

760 **Competing interests.** The authors declare that they have no conflict of interest.